PIV-based investigations of animal flight

Geoffrey R. Spedding · Anders Hedenström

Abstract An overview is presented of the principles of estimation of fluid forces exerted upon solid bodies, based upon whole-field velocity measurements such as provided by PIV. The focus will be on the range of length and velocity scales characterised by the flight of large insects, birds, bats and small unmanned air vehicles, so that while viscous terms in the Navier–Stokes equations can many times be ignored in the quantitative analysis, understanding and measuring boundary-layer flows, separation and instability will ultimately be critical to predicting and controlling the fluid motions. When properly applied, PIV methods can make accurate estimates of time-averaged and unsteady forces, although even ostensibly simple cases with uncomplicated geometries can prove challenging in detail. Most PIV-based force estimates are embedded in some analytical model of the fluid–structure interaction, and examples of these with varying degrees of complexity are given. In any event, the performance and accuracy of the PIV method in use must be well understood as part of both the overall uncertainty analysis and the initial experimental design.

G. R. Spedding
Department of Aerospace and Mechanical Engineering,
University of Southern California, Los Angeles, USA

Present Address:
G. R. Spedding (✉)
Department of Mechanical and Aeronautical Engineering,
University of Pretoria, Pretoria 0002, South Africa
e-mail: geoff.spedding@up.ac.za

A. Hedenström
Department of Theoretical Ecology, Lund University,
Ecology Building, 223 62 Lund, Sweden

List of symbols

A	tip-to-tip flapping amplitude (m)
AR	aspect ratio ($AR = b/c$)
b	wingspan (m)
c	mean chord (m)
C_L, C_D	lift and drag coefficients ($C_x = F_x/qS$)
$C_{D,pro}$	profile drag coefficient of wing
$C_{D,i}$	induced drag coefficient of wing
C_F	laminar skin friction coefficient
D	image displacement (pix)
D	drag, force parallel to U_0 (N)
D'	drag per unit span (N/m)
f	flapping frequency (/s)
F_x	force component in the x direction (N)
$\mathbf{g}$	acceleration due to gravity (m/s^2)
I	impulse (kg m/s)
l	length scale (m)
L	lift, force normal to U_0 (N)
p	pressure (N/m^2)
p_0	freestream pressure (N/m^2)
q	dynamic pressure ($q = \frac{1}{2}\rho U^2$, N/m^2)
Re	Reynolds number (Re_x based on length scale x)
r_0	vortex radius (m)
$\mathbf{R}$	general, resultant force vector (N)
R_{wv}	wake vortex ratio
S	control surface (m^2)
S	shear deformation (dx/x, dimensionless)
S	wing planform area ($S = bc$, m^2)
St	Strouhal number ($St = fA/U$)
t	time (s)
T	wingbeat period (s)
$\mathbf{u}$	velocity vector field (m/s)
u, v, w	velocity components in x, y, z (m/s)
u_1	upstream uniform streamwise velocity (m/s)
u_2	downstream, disturbed streamwise velocity (m/s)

U_0	mean, undisturbed uniform streamwise velocity (m/s)
U	mean flow speed or mean flight speed (m/s)
V	control volume (m^3)
w_i	induced velocity (due to wing lift) (m/s)
W	body weight (N)
$\mathbf{x}$	position vector (m)
x, y, z	Cartesian coordinates in streamwise (flightwise), spanwise and vertical directions (m)
α	angle of attack (deg)
α_i	induced angle of attack—the decrease in α caused by w_i (deg)
δt	exposure time between two PIV images (typically µs)
ϕ	velocity potential (m^2/s)
Γ	circulation (m^2/s)
Γ_0	circulation at wing centreline (m^2/s)
μ	viscosity (kg/m/s)
v	kinematic viscosity ($v = \mu/\rho$, m^2/s)
θ	momentum integral (m)
ρ	fluid density (kg/m^3)
$\boldsymbol{\omega}$	vorticity vector (/s)
ω_x	vorticity component in the x direction (normal to the yz plane) (/s)

Abbreviations

CIV	Correlation Imaging Velocimetry
DLE	Direct Lyapunov Exponent
DNS	Direct Numerical Simulation
ENOB	Effective Number of Bits
LCS	Lagrangian Coherent Structure
LEV	Leading Edge Vortex
PIV	Particle Image Velocimetry

1 Introduction

Particle image velocimetry (PIV)-based methods have been successfully used to show the airflows induced by the flapping wings of animals in free and tethered flight, and by fixed mechanical model flappers, and they feature in the majority of papers in this special issue. PIV can provide robust estimates of instantaneous velocity fields, which are often shown in conjunction with the vorticity component normal to the plane of measurement to describe complex and time-varying flows. Time-resolved PIV can also be used to estimate acceleration terms in the Navier–Stokes equations, and can then support alternative structure identification algorithms and/or compute instantaneous forces. In all of these cases, a correct quantitative analysis requires the performance characteristics of the particular method be well understood under realistic experimental conditions.

Here we give an overview of the principles of calculation of time-averaged and instantaneous forces from PIV-based measurements of the velocity field. We begin by examining the equations of motion for uniform incompressible fluids to provide a basis for quantitative analyses based on different properties of the measured flow fields. Two classes of measurement are considered—those based on integral momentum measures and those deriving from the observed structure of the vorticity field, and the strengths and limitations of PIV-based data in each will be noted. Selected examples will be given for fixed wings and for flapping animal flight. Increased sophistication may come either from reducing the number and/or scope of assumptions in the analysis, or changing their form. Improvements in analytical techniques will proceed simultaneously with predictable advances in technology, some of which are outlined.

1.1 Momentum and vorticity equations

The momentum equation for an incompressible fluid continuum of uniform density is

$$\rho \frac{D\mathbf{u}}{Dt} = \rho\mathbf{g} - \nabla p + \mu\nabla^2\mathbf{u}, \tag{1}$$

where the acceleration of a material volume of fluid is determined by the rate of generation of momentum by surface and volume forces on the right hand side. When the density, ρ, and viscosity, μ, are constant, then fluid motions, $\mathbf{u}$, are altered due to gradients in the pressure, p, and by viscous shear stresses. The Navier–Stokes equations (Eq. 1 plus a mass conservation equation) are notoriously rich in their range of possible solutions, and at the same time, experimental determination of all the terms is difficult.

The solutions of Eq. 1 can be characterised by the Reynolds number, $Re \equiv ul/v$, where u and l are characteristic velocity and lengthscales, and $v = \mu/\rho$. In many animal flight studies, Re based on a mean wing chord, c, lies between 10^3 and 10^5. This is a particularly interesting range: at the high end ($Re = 10^5$), viscous effects can almost be ignored and many classical aerodynamic theories work perfectly well. At the lower end ($Re = 10^3$), viscous effects come to predominate and ensure a degree of stability and predictability of the thick boundary layers that are formed over even quite odd-shaped bodies. In between, we pass through a regime where certain quantitative predictions of inviscid theory work very well, but where one can also find very large qualitative changes in flow fields that ultimately depend on the boundary layer behaviour. In the examples that follow, we will at times simultaneously ignore all viscous contributions to Eq. 1 and yet still seek physical explanations that depend on viscosity. The experimental domain is comparatively simple for PIV

studies—there are no significant compressibility effects and no Brownian motions at small scale to worry about. Measurement success instead usually hinges on the degree to which time-varying and/or three-dimensional flow fields can be appropriately simplified. As we shall see, this is even true for a rigid, fixed, nominally two-dimensional airfoil, which can easily be shown to induce a three-dimensional, time-varying velocity field.

While the value of Re determines the relative magnitude of the terms in the governing Eq. 1, and its descendents, the PIV methods and principles outlined here apply rather the same from fruit flies to geese (or models thereof).

In the search for appropriate simplifications, the momentum equation can be re-expressed in various ways. For example, Eq. 1 can be written

$$\frac{\partial}{\partial t} \int (\rho \mathbf{u}) \, dV + \int (\rho \mathbf{u}.dS) \, \mathbf{u} = \int \rho \mathbf{g} \, dV - \int p \, \mathbf{dS} + \int \mu \nabla^2 \mathbf{u} \, dV, \tag{2}$$

where the integrals are taken over a volume V enclosed by a surface S. The interest in these integral forms is that momentum fluxes in one part of the fluid can be calculated given conditions in another part, without needing to know details of the flow in between. This forms the basis for control volume methods and the force balance estimation that appears later. From an experimental point of view, we may note that integral quantities can frequently be estimated more robustly than derivatives.

Taking the curl of both sides of Eq. 1, gives the vorticity equation

$$\frac{D\boldsymbol{\omega}}{Dt} = \boldsymbol{\omega}.\nabla \mathbf{u} + \nu \nabla^2 \boldsymbol{\omega}, \tag{3}$$

where $\boldsymbol{\omega} = \nabla \times \mathbf{u}$ is the vorticity, and writing the equation in this form is interesting for at least two reasons. First, the pressure does not appear in Eq. 3, and it is only viscous shear stresses (and not the normal stresses) that can modify the angular momentum of a fluid element. Second, for moderate- to high Reynolds number, it can be convenient to describe the flow field in terms of the vorticity distribution, since in the inviscid limit there are conservation laws governing the behaviour of vortex elements. In particular, if the circulation, Γ, around a closed material curve is written

$$\Gamma(t) = \oint \mathbf{u}.\mathbf{dS}, \tag{4}$$

then Kelvin's circulation theorem shows that Γ is constant:

$$\frac{d\Gamma(t)}{dt} = 0. \tag{5}$$

If the closed integration curve bounds a material surface, S, then

$$\frac{d}{dt} \int \boldsymbol{\omega}.\mathbf{dS} = 0, \tag{6}$$

and a vortex tube within S has constant strength and moves with the fluid. The convenience of these representations encourages measurement and analysis of flow fields in terms of the vorticity field, with the added experimental advantage that once again Eq. 4 is an integral measure, which can in principle be robustly measured, provided that the appropriate surface S can be identified.

1.2 Characteristics and limits of PIV

Particle Imaging Velocimetry (PIV) methods are concerned with measuring both displacement fields and their spatial gradients, and close attention must be paid to the likely errors in estimating both in any given experiment. Here we summarize (and simplify) arguments advanced in Fincham and Spedding (1997) concerning the limits in PIV. For any PIV algorithm, there will be a fundamental lower limit in resolution of small displacements, D. This lower limit is almost always set by the severity of peak-locking errors in a given practical experiment (as opposed to an idealized numerical simulation). Peak-locking is the tendency of a correlation extremum to be resolved close to an integer number of discretisation steps. It has been discussed in Fincham and Spedding (1997), Westerweel (1997), Westerweel 2000), Prasad et al. (1992), Nogueria et al. (2001), Chen and Katz (2005) and Cholemari (2007), amongst others. A reasonable algorithm ought to be able to resolve displacements of better than 0.02 pixels. Since the algorithm error is fixed in pixels (it does not vary with D), and if the maximum tolerable (or claimed) error is 10%, then the minimum resolvable displacement $D_{min} = 0.2$ pixels. To measure a broad range of scales, one then searches for the largest possible D_{max}, set by

$$D_{max} = u_{max} \delta t, \tag{7}$$

where δt is the PIV exposure time between successive images. u_{max} is set by the flow and the only remaining control variable is δt. However, increasing δt also increases the local shearing deformation as

$$S = \omega \delta t. \tag{8}$$

It is for this reason that codes including box deformation (e.g. Huang et al. 1993; Scarano and Riethmuller 1999; Fincham and Delerce 2000; Scarano 2002) can offer significant practical improvements in performance (as recently confirmed by Stanislas et al. 2008). Further practical limits on δt derive partly from curvature of local pathlines which leads to significant and systematic errors in velocity estimation, and partly because very few flows are simple enough to confine their motions to a light

sheet, or light slab, for long times. (This discussion assumes simple PIV experiments, where displacements are observed within a plane. The use of 3D or stereoscopic methods modifies this latter argument.) Finally, increasing D_{max} leads inevitably to reduced spatial resolution because the result is an average over D_{max}, and reduced temporal resolution as accelerations over δt are lost.

As a very rough rule of thumb, we can suppose that the sum of these effects can be expressed conservatively as a constraint that $D_{max} = 5$ pixels. If $D_{min} = 0.2$ pixels, the bandwidth of measurable velocities within 10% uncertainty is 25. The arguments leading to this number are approximate, and numerical details can be modified by advances in technique (box deformation, multipass analysis algorithms, multiscale acquisition procedures) but the basic principles apply quite generally. In a general review, Adrian (2005) notes that due to the low dynamic range, most PIV investigations are primarily exercises in optimization.

Because the bandwidth is low (compared with LDA or hot-wire measurements, for example), and limited on the D_{min} side by algorithm errors, the strong interest in development of more sophisticated fundamental PIV algorithms persists, more than 15 years after the first digital PIV techniques were described (Utami and Blackwelder 1991; Willert and Gharib 1991). In any given system, the constraints on D_{max} and S_{max} in determining u_{max} and ω_{max} in Eqs. 7 and 8 require a very careful selection of δt. Finally, a meaningful measurement of velocity or gradient fields requires a sound quantitative knowledge of the likely measurement error and its distribution.

1.3 Objectives

The purpose of this paper is to illustrate the experimental estimation of terms in the various forms of the momentum equations, using appropriate PIV methods. Whilst all examples given will use the correlation imaging velocimetry (CIV) algorithms described in Fincham and Spedding (1997) and Fincham and Delerce (2000), the lessons and limitations are general and apply to all PIV measurement schemes. Two types of experiment/measurement are considered. The first involves an application of control volume methods suggested by Eq. 2 for an ostensibly simple flow—steady uniform flow over a flat plate, fixed at various angles of incidence. The analysis is guided by quite strong approximations from aerodynamic theory and estimated forces from PIV analysis can be compared with those measured directly by a force balance. The second example is much more complicated—in principle. We wish to make quantitative measurements of the disturbances in the wake of an animal in flapping flight. The integral momentum Eq. 2 again provides the

framework for inferring average forces on the complex, time varying wing shapes by analysis of the far wake. The wake itself is described by its vorticity field, and by using circulation measures of the total strength of simple geometric approximations of the wake structure, force balance calculations can again be attempted. The results shed some light on future research strategies and on the correctness of the modeling approximations used in the analysis.

2 Control volume methods

2.1 Calculating drag from the time-averaged wake momentum defect

The calculation of the drag on a solid body immersed in a uniform flow field by estimating the momentum defect magnitude in the wake appears to have been first considered carefully by Betz (1925), which formed the basis for the treatment by Prandtl and Tietjens (1934). The principles can be found in any fluid mechanics textbook (e.g. White 2008) and are summarized here to clarify the assumptions and relation to the equations of motion given in the Introduction.

Figure 1 shows an airfoil section in a constant uniform flow, $u_1(z) = U_0$. A control volume, V, is defined by enclosing the airfoil within a streamtube with surface contour S. If viscous forces are neglected, then Eq. 2 becomes

$$\frac{\partial}{\partial t} \int (\rho \mathbf{u}) \, dV + \int (\rho \mathbf{u} . \mathbf{dS})\mathbf{u} = -\int p \, \mathbf{dS} - \mathbf{R}, \qquad (9)$$

where $\mathbf{R}$ is the resultant force exerted on the control surface by the normal and shear stresses acting at the airfoil surface. If the flow is further assumed to be steady, and if S is taken sufficiently far from the airfoil so that the pressure there is equal to the constant, undisturbed freestream pressure, p_0, then Eq. 9 reduces to
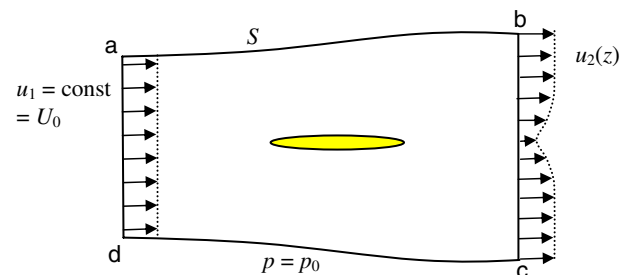

Fig. 1 Control volume around a solid body in a uniform freestream. A constant uniform flow, u_1 appears through the face *ad*, and the streamtube, *S*, that surrounds this flow is cut at face *bc* behind the body. The force on the body is equal to the change in momentum flux between $u_2(z)$ at *bc* and uniform u_1 at *ad*. The pressure, *p*, on the streamtube boundary is equal to the undisturbed pressure, p_0

$$\mathbf{R} = -\int (\rho \mathbf{u}.dS)\mathbf{u}. \tag{10}$$

If we consider only the streamwise component of the force, the drag per unit span (the control volume V has unit span in the out-of-plane direction), D' is

$$D' = -\int (\rho \mathbf{u}.dS)u. \tag{11}$$

Because S lies along streamlines in the flow, the only contribution to the momentum flux is from the flow in through the front surface and the flow out through the rear surface, and the integral in Eq. 11 is

$$\int (\rho \mathbf{u}.dS)u = -\int_d^a \rho_1 u_1^2 \mathrm{d}z + \int_c^b \rho_2 u_2^2 \mathrm{d}z. \tag{12}$$

When $u_1 = U_0$ and ρ are constant, the total (positive) drag of a body with span b can be expressed as

$$D = \rho U_0^2 b \theta, \tag{13}$$

where the momentum integral,

$$\theta = \int_c^b \left(\frac{u_2}{U_0} - \left(\frac{u_2}{U_0}\right)^2 \right) \mathrm{d}z \tag{14}$$

has units of length. If a drag coefficient C_D is defined as D/qS, where q is the dynamic pressure, then

$$C_D = \frac{2\theta}{c} \tag{15}$$

for a wing of chord c and planform area $S = bc$. Equation 14 is simple to evaluate in an experiment, involving only the integration of profiles of the streamwise velocity.

2.2 Estimating the drag of a fixed wing at moderate Re

Estimating the fluid dynamic drag on objects at moderate Re in the range 10^4–10^5 is of particular interest because of recent developments in small-scale flying devices. The forces involved can be small (~ 1 mN) and the flow is easily disrupted by the presence of measuring devices. The following is an example of the simplest possible aerodynamic drag measurement, on a flat plate. The PIV-derived results can be compared with force balance data and with theoretical predictions for a laminar boundary layer.

2.2.1 Steady drag from PIV wake data

Figure 2 shows the flow behind a flat plate at $Re_c = 11{,}700$ (Re_c is based on chord length, c. It is the default definition here and subscript c will be dropped unless required.), and $\alpha = 5°$ which is the angle of maximum lift to drag ratio (L/D). The flow is shown at mid-span and the plate is bounded by vertical end plates aligned with the freestream. The trailing edge of the flat plate is immediately to the left of the picture. $\omega_y(x, z)$ is mapped onto a discrete ten-step colorbar, which matches the likely uncertainty in its determination so measurement errors will not be seen beyond isolated single-color patches. The number of vectors per coherent structure is not large (5–10 per length scale, l_{cs}), and the CIV algorithms were tuned to recover the peak vorticity and velocity peaks in the wake with small deforming correlation boxes. (The correlation box size, B, was reduced in incremental steps to 12 pixels on a side. In CIV, B is independent of any search box scale, S, but B cannot be reduced without limit as the pixel information content decreases with B^2. See Fincham and Spedding (1997) for basic details and Fincham and Delerce (2000) for the removal of shear-generated box deformation as a significant source of error for small B.) The small box size comes at the expense of increased amplitude peak-locking errors in the far field, but they do not exceed the $0.1|\Delta\omega|$ colourbar stepsize (by design). The wake is not steady and uniform, but is composed of coherent patches of vorticity, which interact and decrease in amplitude with increasing downstream distance. The 5-second time average in Fig. 2b shows a smooth wake profile with significantly lower amplitude than the instantaneous field.

The box covering the right side of Fig. 2b shows a region within which mean (row-averaged) velocity profiles were made for all angles of attack and three are shown in Fig. 3, corresponding to the zero-lift ($\alpha = 0$) condition, $(L/D)_{max}$ and $\alpha = 10°$, which is significantly beyond stall, which is abrupt for this shape at this Re. The profiles in Fig. 3 represent the mean momentum defect in the flow due to the presence of the airfoil. As noted in the caption, the profiles have actually been computed as difference profiles, so the far field values fluctuate around $u_X = 0$. Now θ, the momentum integral can be evaluated in each to estimate the x-component of the force. The lift can be seen directly as a deflection of the profiles, which is maximum in this plot at $(L/D)_{max}$. From the PIV processing point of view, the $\alpha = 0°$ profile has only 13 points across it, and estimating its correct magnitude is of great importance. Again, processing parameters are set so to minimising the likely error in resolving the velocity peak and its gradients, but with the side-effect that small ripples in the tails of the distribution can be observed. The tails have zero mean value however, and make no net contribution to θ.

If the flow were perfectly steady and two dimensional, then the momentum flux could be calculated at any plane through Fig. 2b, and an alternative to constructing profiles that are averaged over both space and time is to take any one of the time-averaged profiles at all x locations and calculate θ on each one. The result is shown in Fig. 4. The curves of $\theta(x)$ in Fig. 4 are flat at small α, and then as α

Fig. 2 Spanwise vorticity, $\omega_y(x, z)$ in the wake of a 2D flat plate. $Re = 11,700$, $\alpha = 5°$. The *top panel* (**a**) shows an instantaneous view, and the bottom panel (**b**) is a 5 s time-average. $\omega_y(x, z)$ is mapped onto a ten step colour bar (*inset*) from $-5U/c$ to $+5U/c$. The box covering the rightmost quarter of $\{x, z\}$ shows the region where mean profiles in Fig. 3 are calculated. The field of view, $\{\Delta X, \Delta Z\} = 3.2c \times 1.6c$. The *arrows* show the magnitude of the disturbance velocity field (with the mean inflow velocity subtracted) scaled to 16 times the displacement vector of the original CIV calculation
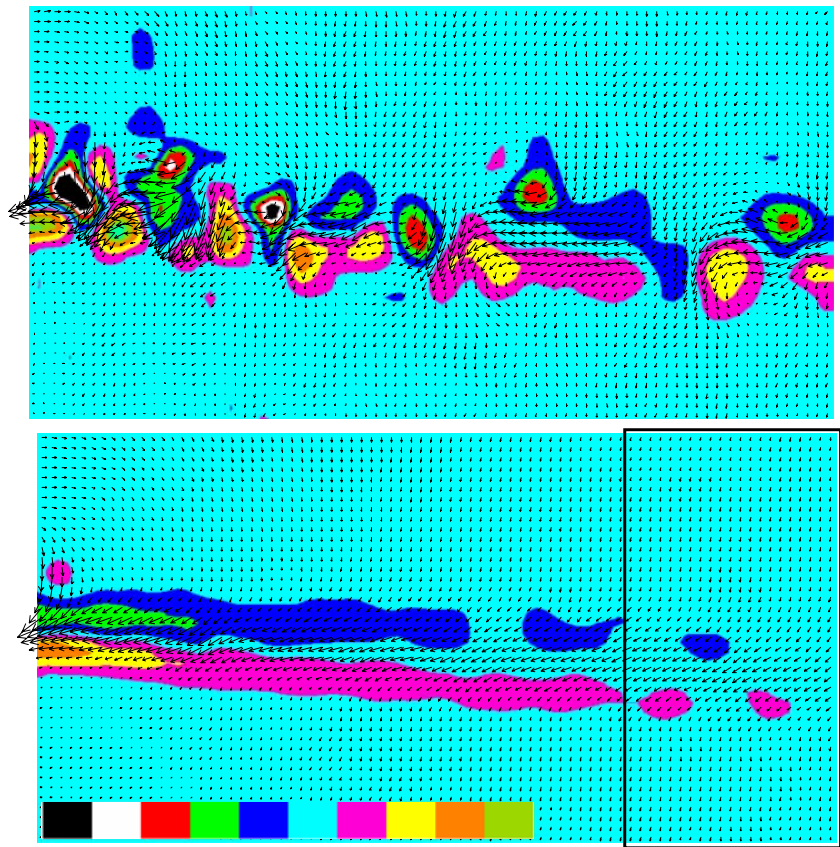
increases, vary significantly with x until they stabilize at $x/c \geq 2$. The systematic variations for small x/c are due to the neglect of the pressure fluctuations in the step from Eqs. 9–10 and the fluctuations on each single profile of $\theta(x/c)$ are due to the unsteadiness of the shedding at the trailing edge. Each single profile cuts through a different section of wake vorticity. Only when the pressure gradients have dropped to small values do the momentum fluxes appear exclusively as differences in the velocity. Fig. 4 suggests that consistent values of C_D require $x/c \geq 2$, and that they will be then independent of x, at least up to $x = 3.2c$. This criterion applies equally to fixed wings and flapping animal flight, as it is unlikely that pressure fluctuations in near wakes of flapping wings will be below those of fixed wings at moderate α. $C_D(\alpha)$ calculated from the PIV-derived wake defect profiles (Fig. 5) shows that the PIV-based measurements agree well with the force balance data for the same aerofoil. The standard deviations in either dataset come from the variation in repeated measurements and are usually smaller than the symbol size. $C_D(\alpha)$ close to $\alpha = 0$ is almost flat.

The analytical result for the total skin friction coefficient of a Blasius laminar profile on a two-sided flat plate is (e.g. Anderson 2001)
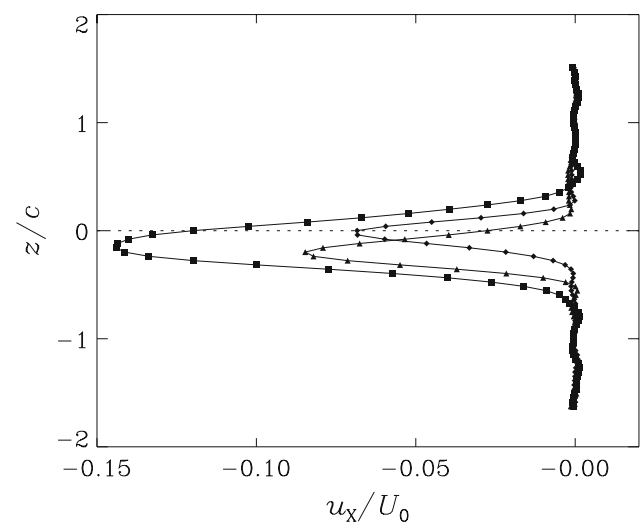

Fig. 3 Mean streamwise disturbance velocity profiles behind the flat plate of Fig. 2 for $\alpha = 0, 5, 10°$ shown by *diamond*, *triangle* and *squares*. Here $u_x(z) = u_{xx}(z) - u_i(z)$, where $u_{xx}(z)$ is the row-averaged streamwise velocity, and $u_i(z)$ is interpolated from a third order polynomial derived from the tails of the distribution only ($z/c \leq -1$ and $z/c \geq +0.5$). $u_i(z)$ is therefore a smooth profile that reflects the acceleration of the mean flow due to blockage effects, and it is assumed that the defect profile rides on top of this baseline. U_0 is the uniform inflow, unaffected by the presence of the airfoil
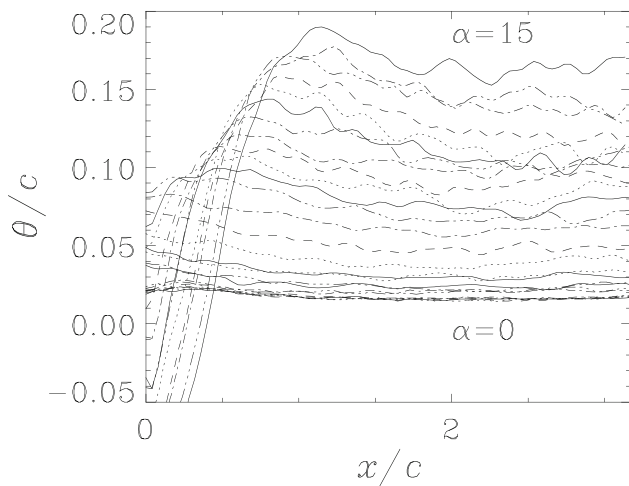
Fig. 4 Equation 14 evaluated with $u_2 = u_X$ from Fig. 3 at different downstream locations behind the flat plate for $\alpha = [-5, 20]$ in 1° increments. The inflow boundary is always assumed to have uniform speed U_0. For $x/c > 2$, θ/c increases monotonically with $|\alpha|$

Fig. 5 Profile drag coefficient measured from PIV experiment (*filled circles*) and the total drag from force balance measurements (*open circles*) as functions of α. C_D is calculated from Eq. 15 where θ comes from a streamwise average over $x/c \in [2, 3.2]$. The horizontal line comes from Eq. 16 for the laminar skin friction over a flat plate

$$C_F = \frac{2.656}{\sqrt{Re_L}}, \tag{16}$$

where Re_L is the Reynolds number based on plate length (so Re_L is based on c). Eq. 16 evaluates to $C_F = 0.0246$ (shown by the horizontal line in Fig. 5). The measured value is $C_D(0) = 0.025 \pm 0.002$, which is the same within experimental uncertainty.

The agreement between PIV measurement and force balance data is a little surprising at large α, when the flowfield is very disorganized and the very large and fluctuating pressure drag component, together with the strongly three-dimensional motion, would combine to contradict many assumptions in deriving the simple expression for θ. Nevertheless, the time-averaged result of the unsteady force is correctly evaluated. Figure 5 shows that 3D corrections are negligible for the 2D flat plate. Strongly three-dimensional geometries and/or small aspect ratio flows may be less easy to summarise in just one measurement plane.

2.2.2 Momentum and energy conservation in far wakes

It is not uncommon in animal experiments for PIV data to be acquired significantly far downstream of the body, and so there is some interest in knowing how far downstream such force balance calculations can be extended. Equation 6 shows that the vorticity is a conserved quantity so it should make no difference. Similarly, Eqs. 5 and 4 show that circulation measurements will also be unaffected. These derivations assume that viscosity is unimportant, i.e. that Re is high. Saffman (1970, 1992)
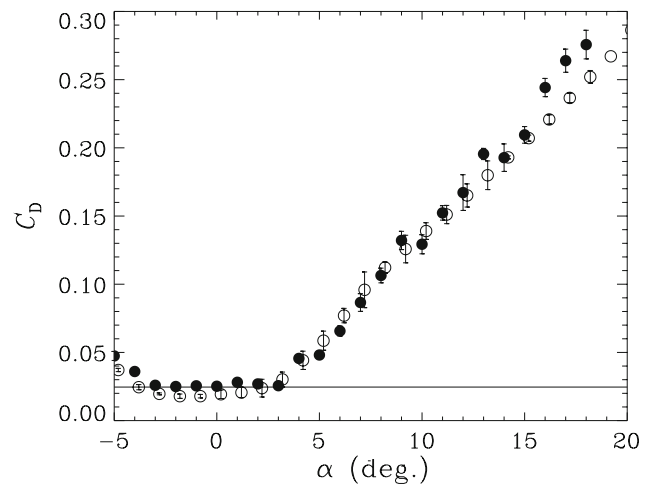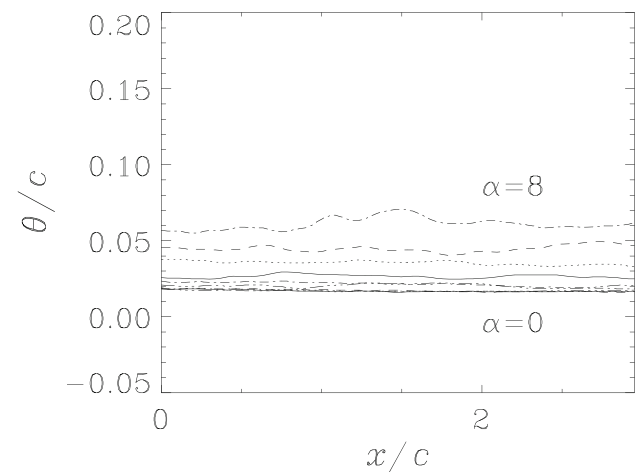

Fig. 6 Momentum integrals from profiles beginning at $x/c = 10$ for an $AR = 6$, rectangular planform flat plate wing from $\alpha = 0$ to $\alpha = 8°$

notes that viscous effects can be considered negligible in vortex rings and wing trailing vortices when the criterion $vt \ll r_0^2$ is satisfied, where r_0 is a vortex radius. Letting the time $t = x/U$, and setting an approximate length scale $r_0 = c$, we require that $x/c \ll Uc/v$. In animal flight experiments, typical x/c values (on the order of 10) are very much smaller than Re_c (on the order of 10^4), and so viscous dissipation should not be important. Indeed, Fig. 6 confirms that θ/c does not decrease significantly from $10 \leq x/c \leq 13$ and that equivalent α generate θ/c of approximately the same magnitude in both Figs. 4 and 6 (the linestyles change in the same order with increasing
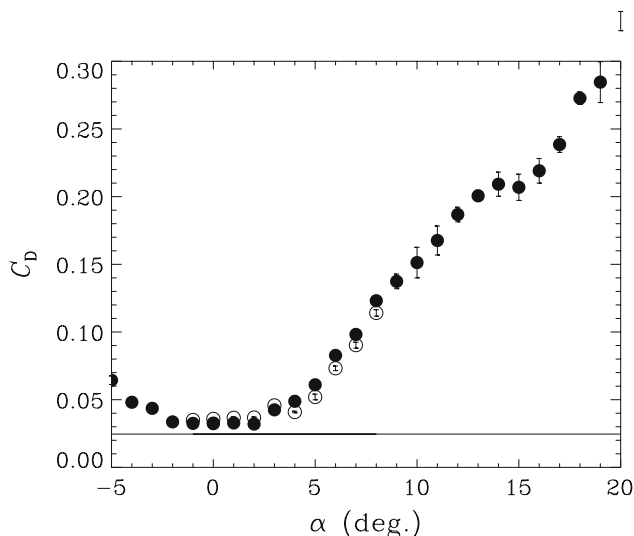
Fig. 7 Particle image velocimetry (*PIV*)-estimated profile drag from the near and far wake of the *AR*6 flat plate. The filled symbols are from streamwise-averaged velocity profiles between $2 \leq x/c \leq 3.2$. The *open symbols* come from profiles averaged over $10 \leq x/c \leq 13.2$. The *solid line* is the 2D flat plate analytical result and the experimental drag estimate is always higher (unlike in Fig. 5) because the $AR = 6$ plate has finite span. The $x = 10c$ data do not extend beyond $\alpha = 8°$

α). The equivalence is only approximate however, as the late wake data in Fig. 6 come from a finite aspect ratio plate ($AR = 6$). At high x/c the wake would be too strongly affected by growing boundary layers at either bounding walls or end-plates, and the latter would be very hard to manufacture, position and align with good accuracy. Thus the most fair comparison is for a finite wing. Figure 7 shows that the drag coefficients calculated from mean velocity profiles starting at $x/c = 10$ are the same as those calculated starting at $x/c = 2$.

2.2.3 PIV versus force balance

Provided the measurements occur sufficiently far downstream so that pressure fluctuations can be ignored, the force-balance and PIV-derived measurements agree very closely. The uncertainty in the wake measurements for C_D is approximately ± 0.002. If the effect of spanwise non-uniformity in the nominally two-dimensional flow field is included (which could be compensated for if other measurement planes were included in the analysis) then a reasonable estimate is that $\Delta C_D = 0.005$, which corresponds to $\Delta D = 0.6$ mN. The force balance is a custom-design cruciform shape with 16 strain gauge elements on the four arms to give two translations and two rotations. The six element calibration matrix was constructed using static weights. When full scale range is ± 10 N, 14-bit

ADCs yield a resolution of 1.2 mN. If the data are over-sampled in the presence of random additive noise, then the estimation of averages can be improved to give a larger effective number of bits (ENOB, Kester 2006). Here, an oversample rate of 8,000 times yields ENOB = 18.5, when the resolution is ± 0.05 mN.

A force balance can be constructed and carefully tuned to robustly and accurately measure the total force on the mechanical system, but the system must include the physical attachment itself. PIV methods are non-intrusive and do not disturb the low-turbulence wind tunnel ambient. They allow the resolution of the forces into different components, but because the pressure is hard to estimate directly, and thin boundary layers are also difficult to resolve, then some simplifying physical assumption (e.g. spanwise uniformity, far fields where $\nabla p = 0$) is usually required.

2.3 Advanced PIV methods for measuring forces

The force estimate for a comparatively simple 2D geometry in a steady mean flow is not complicated, and Figs. 4, 5, 6 and 7 show that the results can be reliable in practice. More sophisticated measurements can take various forms. One is the tighter integration of measurement and theoretical modeling. For example, in classical aerodynamics, one may describe the total drag on an aerofoil as the sum of a profile drag and an induced drag, so

$$C_D = C_{D,\text{pro}} + C_{D,i}. \tag{17}$$

A force balance always measures C_D. The wake measurements of Fig. 5 and 7 measure $C_{D,\text{pro}}$, and the two are equal only in the particular case where $C_{D,i} = 0$ for a two dimensional wing between endplates. If the endplates are removed, $C_{D,i}$ can be estimated by subtraction. Note that there are differing definitions of this rather benign-looking equation that can cause considerable confusion. One common variant assigns to $C_{D,i}$ all of the drag that varies with α.

$C_{D,i}$ is caused by the downwash, w_i, on the wing which, for an elliptically-loaded wing of span b, is constant, and proportional to the bound circulation, Γ_0 (e.g. Anderson 2001),

$$w_i = \frac{-\Gamma_0}{2b}. \tag{18}$$

For small values of the induced angle of attack, α_i, one can write,

$$\alpha_i = \frac{-w_i}{U} = \frac{C_L}{\pi AR}, \tag{19}$$

where $AR = b/c$ is the wing aspect ratio, and so the lift coefficient can be calculated from w_i:

$$C_{\mathrm{L}} = -\frac{w_i A R \pi}{U}. \tag{20}$$

w_i at the wing is constant for an elliptic load distribution but PIV measurements can measure w_i across the wing length. In wing theory half of the induced downwash occurs at the wing and half again behind it, so measurements in the Trefftz (y, z) plane taken in the far wake will give estimates of $2w_i$, which can in turn be used to calculate the lift on the wing through Eq. 20. Spanwise distributions of $w_i(y)$ behind the hindwing of a tethered locust derived from multiple PIV sections in streamwise planes, taken at $x \approx b/2$, are shown in Bomphrey et al. (2006), but the integrated instantaneous lift of approximately ten times the body weight was not easily reconciled.

The relationships in Eq. 15 and (17–20) show how the lift and drag components of a wing in steady flow can be calculated from quite simple wake measurements, although Eq. 17 has some subtleties that are not immediately obvious. Meheut and Bailly (2008) have shown how quite different numerical results can come from example wake surveys that were simulated through a computed direct numerical simulation (DNS) through integration of a discretised Eq. 1 flowfield, depending on details of the physical assumptions behind Eq. 17 or equivalent.

Particle image velocimetry has also been used to estimate forces in more complex geometries and in time-varying flows. Re-arranging Eq. 9, the force **R** on a body immersed in an inviscid fluid is

$$\mathbf{R} = -\frac{\partial}{\partial t}\int (\rho\mathbf{u})\,\mathrm{d}V - \int (\rho\mathbf{u}.dS)\mathbf{u} - \int p\,dS, \tag{21}$$

and so can be computed given a time-resolved velocity field inside a control volume and a pressure distribution at the volume surface. The pressure can be estimated from the velocity field, so neglecting viscous terms in Eq. 1 for convenience (this is not a necessary step),

$$-\nabla p = \rho\frac{\partial\mathbf{u}}{\partial t} + \rho(\mathbf{u}.\nabla)\mathbf{u} \tag{22}$$

and the pressure field is calculated by integration from some known boundary condition. Lin and Rockwell (1996) and Noca et al. (1999) have used time-resolved PIV fields using control volume methods with different techniques for estimating the pressure. The PIV requirements are quite stringent, because both velocity gradients and accelerations in Eqs. 22 and 21 must be calculated to good accuracy. We note that the examples given here have side-stepped all problems arising in resolving velocities and their gradients close to solid (possible moving and deforming) boundaries, by concentrating exclusively on far wake measurements, where the pressure gradients in Eq. 22 are small.

By contrast, Van Oudheusden et al. (2007) made time-averaged force estimates by calculating all the required terms in the momentum equation from velocity and pressure gradient fields where time-averaged pressure gradients were calculated from velocity and Reynolds stress gradients. The agreement with direct force measurement on a 2D square cylinder in a steady uniform flow was reasonable. They also measured mean lift and drag coefficients on a NACA 642A015 section at $Re = 3 \times 10^3$ and obtained better agreement in drag measurements when a single wake transect formed the basis of pressure and velocity measurements than when an exterior contour was used to calculate a form of Eq. 21.

Since animals have no rotating machinery at the macroscale (the plumbing required to support living tissue would be difficult to arrange), they have no continuously rotating propellers or turbines, and their locomotory force generators always involve reciprocal cyclical motion of propulsive elements. This means that the fluid motions and associated forces are always time varying—it is simply a question of the relative magnitude of the $\partial/\partial t$. term in Eq. 21, for example. There are two consequences of this: first, it may be very difficult to choose an appropriate control volume in animal studies. Having highly trained, repeatable motion, without net acceleration over one periodic propulsive cycle (if such behaviour exists) certainly helps, but the far-field boundary conditions may still not be easy to verify, and one need only look at the engineering examples given in the preceding paragraphs to appreciate the complexity already offered by a fixed, non deformable bluff body in steady flow.

The second complication that comes from the unsteady motion is that although the vorticity equation (3) successfully eliminates the pressure, the nonzero unsteady term can be shown (Saffman 1992) to lead to the following relationship between the force **R**, and the vorticity, **ω**:

$$\mathbf{R} = \rho\frac{\partial}{\partial t}\int \mathbf{x}\times\boldsymbol{\omega}\,\mathrm{d}V + \rho\frac{\partial}{\partial t}\int \phi\mathbf{n}\,\mathbf{dS}. \tag{23}$$

x is a position vector, **n** is the surface normal to S, and ϕ is the velocity potential. The force now depends on the acceleration of a potential flow (second term on rhs of Eq. 23), as well as the strength of vortex elements in the flow (first term). If a vortex element is immersed in an unsteady potential flow field then there will be an extra force that acts like an added mass on the vortex element itself, and it is not necessarily sufficient to calculate forces from flow fields that are derived, either implicitly or explicitly, from the vorticity field alone. Dabiri (2005) first explained this in the context of animal swimming and flying and proposed a wake vortex ratio, R_{wv}, (subsequently corrected and modified in Dabiri et al 2006, Appendix) that essentially depends on the ratio of the

velocity increment of the accelerating background potential flow to the self-induced translational velocity of a vortex element. In far wake studies of bird flight R_{wv} has too small a value to merit the inclusion of vortex added mass terms (e.g. Hedenström et al. 2006), but this is likely not the case in near wakes with significant unsteadiness. The proper resolution of the fluid accelerations then will require time-resolved PIV data.

The combination of time-resolved PIV and integrated theoretical models shows great promise in accurate and non-intrusive measurement of instantaneous forces on bodies in homogeneous fluids.

3 Flight of birds and bats

We have noted above how theoretical models can guide applications of PIV measurement plans to estimate time-averaged and instantaneous forces without interference in the flow itself. Here we show two examples where such advantages are prerequisites, in the study of the free flight of birds and bats. The examples will show ways in which common aerodynamic assumptions can be used to estimate wing properties from measurements that are reasonable given the measurement uncertainty. We emphasise the PIV constraints in running such experiments to show general principles.

A number of birds and bats have been studied in the Lund University wind tunnel, and a recent review of the experiments can be found in Hedenström and Spedding (2008). Here we show two contrasting examples.

3.1 Swifts

3.1.1 The basic experiment

Swifts represent an extreme example of aerial specialisation as they are thought to fly continuously, landing only to nest, from their first flight. Their flight involves flapping, gliding and sharp turns and their wings are rather rigid,

with a characteristic crescent-moon planform that has long been known to be efficient in fish propulsion (Lighthill 1970). One fledgling swift was captured in its nest and made its first ever flight in the wind tunnel (Henningsson et al. 2008), learning quickly to fly reliably and repeatedly in the centre of the test section.

The closed-circuit, low turbulence wind tunnel was filled with fog particles of about 1 μm diameter, and the wake downstream of the flying bird was sampled in vertical streamwise planes at various points in the spanwise direction. The sampling rate, limited by the Nd:Yag laser, was 10 Hz, which is comparable to the wingbeat frequency of 8–9 Hz. The small phase difference between successive wake samples can thus be used to assemble contiguous sequences of images that together sample one complete wake wavelength, as shown in Fig. 8.

Figure 8 shows that spanwise vorticity is shed continuously into the wake, with positive-signed vorticity being shed at the beginning of the downstroke, and mostly negative-signed vorticity during the upstroke. The transition between the two phases is gradual and consistent with a gradually increasing bound circulation on the wing (and lift) on the downstroke followed by a decreasing circulation on the upstroke. Since the changes in wake circulation can be quantified then these can be used to infer conditions on the wing (with the necessary condition of Kelvin's circulation theorem, Eq. 5) and to calculate a wake impulse, I, that must support the weight, W, of the swift over one period, T, of the wingbeat:

$$I_z = WT, \tag{24}$$

where the subscript z denotes the vertical component of the total impulse. Taking I_z over T in this way is correct if there are no net accelerations (in any direction) over one wingbeat. Data were only used when sequences of gradually changing wake phase showed that the vertical position was steady. The other two directions are harder to verify (although the swift position was monitored in synchronised video from a downstream camera), except that anomalies in the wake structure can always be seen
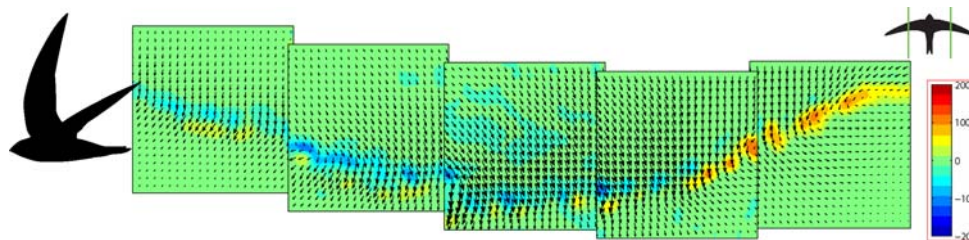

Fig. 8 A reconstruction of one wake wavelength from a swift in steady level flight at 8.4 m/s. The *colour map* shows the spanwise vorticity, which is zero, within experimental uncertainty, in most places. The thin undulating trail of nonzero vorticity approximately follows the wing trailing edge at that section (around mid-span— *inset*). The trailing vorticity does not aggregate into discrete clumps, changing only gradually from positive at the beginning of the downstroke (*upper right*) to negative at the beginning of the upstroke (*middle*). From Henningson et al. (2008)

before the signature of a significant wake/position variation is observed. Such anomalous sequences are never included in the statistics/analysis. The slow and predictable variation in wake phase over successive wingbeats acts as a very useful (and initially entirely unintentional) check on the steadiness of each flight sequence. The experiment was repeated over a number of spanwise locations, nb, and at each one, the wake was divided into a number of streamwise sections, $n\phi$. Then the wake impulse can be calculated from

$$I_z = \rho \sum_{i=1}^{n\phi} \sum_{j=1}^{nb} \Gamma_{ij} S_{ij}, \qquad (25)$$

where the S and Γ are the projected areas and circulations of each wake panel. The time-averaged vertical force, $F_z = 0.43 \pm 0.13$ N, and the weight of the swift, $W = 0.38 \pm 0.05$ N. The two values are the same within experimental uncertainty.

3.1.2 Measurement uncertainty

The uncertainty in F_z comes from the variation of multiple wake panels from all measured flights. It includes contributions from the basic measurement uncertainty in Γ. Although the PIV processing parameters (particularly the correlation box size) were selected to correctly resolve velocity gradients, at the possible cost of incurring peak-locking errors, Γ is not affected by the peak-locking errors in low amplitude regions (like the tails of the distributions in Fig. 3) because it is a thresholded quantity. Note that an accurate estimate of the velocity gradients and derived quantities requires a careful choice of δt, within the constraints of Eqs. 7 and 8. δt is here tuned not to the mean flow, which is removed as a constant by shifting the entire correlation calculation, but to disturbance quantities about this mean. In this way the limited PIV bandwidth is used more fully. ΔF_z also depends on the variability of the bird flight patterns, and very rigorous and careful conditions are required so that these contributions do not dominate the measurement.

The PIV processing parameters together with the original experimental conditions that include δt, must be carefully chosen if distributions of $\omega_y(x, z)$ such as Fig. 8 are to be trusted. Since there is no error-free measurement, then the estimated field should be represented in discrete steps where the step size is related to the measurement uncertainty. Figure 8 does this, and it is worth enquiring whether the wake structure is similar to that expected behind more usual wing shapes at similar Re.

3.1.3 Comparison with fixed wings

Re_c of a swift in cruising flight is about 2.2×10^4, and Fig. 9 shows the wake behind a cambered, circular arc section for $Re = 1.2 \times 10^4$. The angle of attack, $\alpha = 5°$ where the cambered plate has a maximum $L/D = 6.8$. The near wake is composed of an ordered sequence of vortices that are more regular in appearance than for the flat plate in Fig. 2. While Fig. 9 shows the near wake up to about 1.5 chord lengths downstream of the trailing edge, the bird data are taken from $x/c = 10$ or more, and the comparatively compact regions of trailing vorticity there suggest that, like the cambered plate below stall in Fig. 9, there is most likely no large scale trailing edge separation on the wing. This would be expected, because the drag cost of having separation at the trailing edge would be high, with no obvious aerodynamic benefit.

Figure 9 shows that the steady flow past the cambered plate is attached (at least at large scale) over the entire

Fig. 9 The spanwise vorticity field, $\omega_y(x, z)$ around and behind a plate with 5% circular arc camber at $Re = 1.2 \times 10^4$ and $\alpha = 5°$. The mean flow, U, from left to right, has been removed. The field of view $\{\Delta X, \Delta Z\} = 2.6c \times 1.2c$

$-8U/c$ 0 $+8U/c$
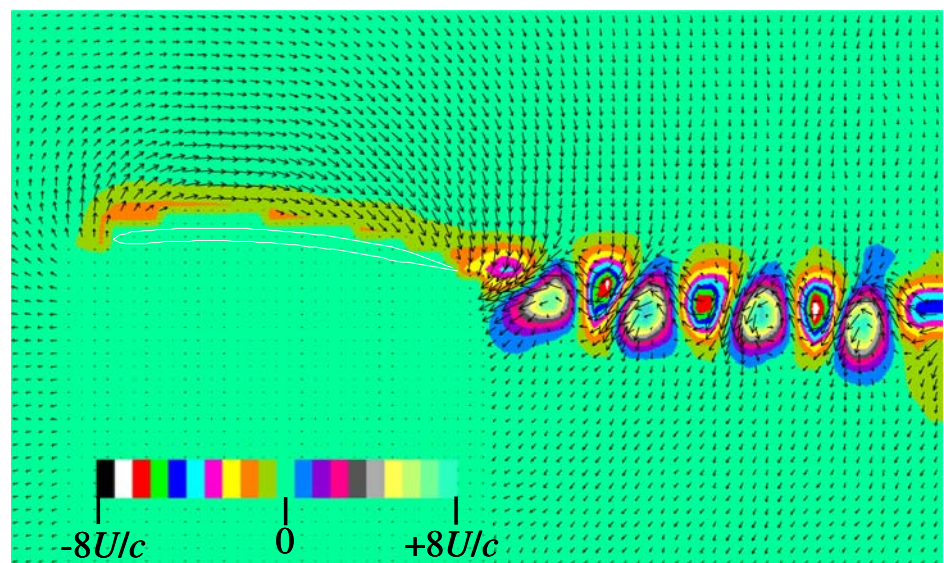
upper surface. That condition is not obvious from inspection of the free wake alone, and it is not clear either how to infer on-wing conditions from far wake measurements such as Fig. 8.

3.2 Bats

3.2.1 Measuring the instantaneous lift from the flowfield on the wing

Bats are known as specialists in manoeuvrable and slow-speed flight, and typically have lower wing loading than similar-sized birds (Norberg 1990). Their wings are composed of an elastic membrane composed of muscle fibres and a supporting collagen matrix, which is stretched between elongated bones that are derived from fingers. The aerodynamic consequences of these differences in wing shape and structure have long been of interest, both to biologists and to engineers contemplating biomimetic designs. Moreover, the role of wing flexibility is of fundamental interest in flapping flight.

Bats have also been investigated in the Lund wind tunnel and intricate patterns in the far wake have suggested (again indirectly, as for the swift) that certain details in the wing aerodynamics during the course of the wingbeat are significantly different from those seen for birds (Hedenström et al 2007). From the far-wake measurements it was unclear what the on-wing differences might be. The first measurements of the flow over the bat wing were made possible by a shroud that automatically masked the eyes of the bat when it came to feed at the nectar feeder (Muijres et al. 2008). This prevented high energy laser light from damaging the eyes. At one point in the wingbeat in slow forward flight (~ 1 m/s), the wing is held outstretched horizontally, roughly 2/3rd the way through the downstroke. At that moment, one can capture and analyse image pairs that show the flow field above the wing surface, much as in Fig. 9 for the cambered plate. Figure 10 shows the first image of a pair, where the bat and particle field have the PIV analysis grid superimposed. The grid is composed of calculation points, boundary points and masked points. The background bat image is reduced in amplitude by applying a high pass filter to the entire image. The CIV processing algorithms (Fincham and Spedding 1997; Fincham and Delerce 2000) calculate displacements at each grid node, and the node point is shifted by one half of the displacement. The now irregularly-spaced vector field is then re-interpolated back onto the original grid and the wing motion is used as boundary-value points for the smoothing spline interpolating functions. The objective is to resolve data as close to the moving wing boundary as possible. Details of the performance analysis are beyond the scope of this review, but an example result is shown in
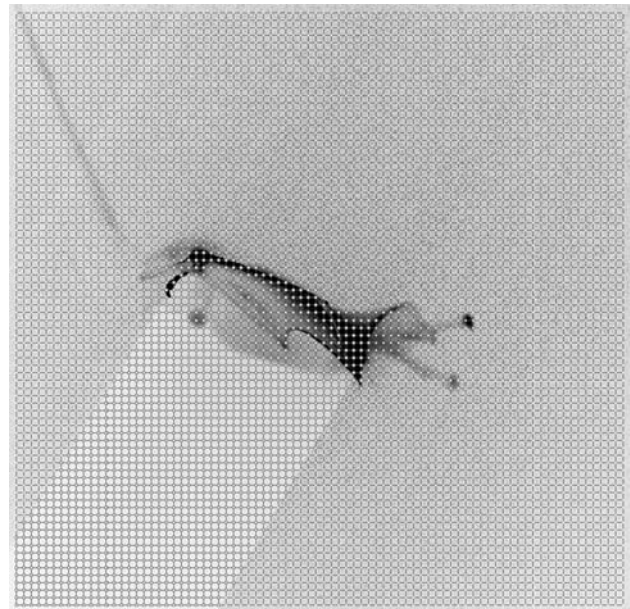

Fig. 10 Inverted grey-scale image of bat and particle field, with PIV analysis grid superimposed. Masked points are shown by *squares* at the grid nodes. Motion of the upper wing surface is calculated to provide boundary conditions to final smoothing spline interpolation back onto this analysis grid

Fig. 11. The original data points shown by crosses are approximated by the continuous line spline functions, whose end conditions are set by the wing motion. The spanwise vorticity,

$$\omega_y(x, z) = \partial w / \partial x - \partial u / \partial z,$$

is determined largely by the large positive values of $\partial u / \partial z$ shown in Fig. 11. A large blob of negative (clockwise rotation) spanwise vorticity lies attached to the upper wing surface (as shown by Muijres et al. 2008), and the strongest gradients in $\partial u / \partial z$ occur above the left third of the wing. The local flow above the membrane is reversed, as shown by the bold symbols. The reversal is due to the influence of the LEV, and to the motion of the wing surface itself, which sweeps from right to left in the wind-tunnel fixed reference frame. The no-slip condition causes the boundary shear profiles, which develop into the near-wake drag defects to the lower right. As the wing accelerates downwards, it also pitches clockwise by rotation about the leading edge, increasing the geometric angle of attack.

3.2.2 An aerodynamic analysis of the LEV

The aerodynamic effect of the leading edge vortex can be estimated in an approach similar to that pioneered by Polhamus (1971) for separation vortices on delta wings. In the bat experiments, the circulation of the trailing vorticity, Γ_{TEV}, is used as a measure of the total wing circulation,
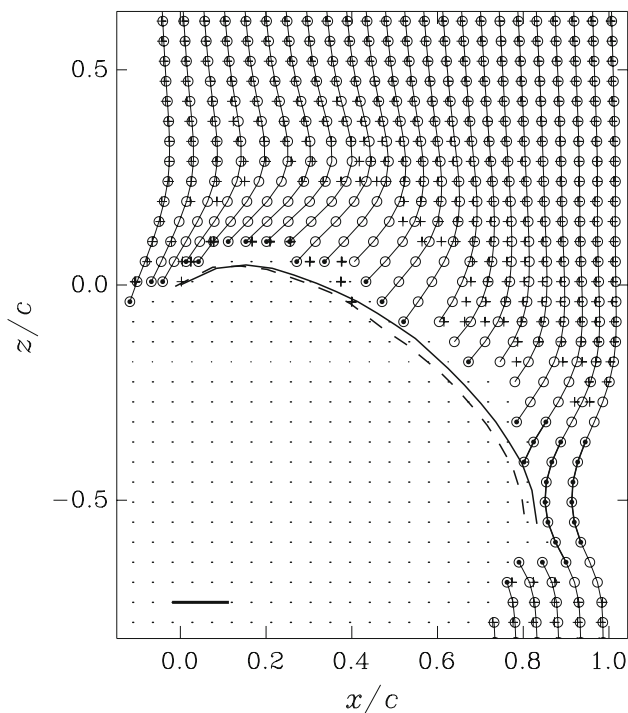
Fig. 11 Velocity profiles above the wing. The original data are shown by *crosses*. The interpolated points are shown by *circles* and *continuous lines*. *Lines* and/or *symbols* are drawn in *bold* when they denote negative velocities (from *right to left*). Displacement profiles are magnified ×5. The *horizontal scale bar at bottom left* shows a 5 m/s displacement, also magnified by ×5. The wing boundary coordinates are shown in straight-line segments for the first image and by *dashed line* for the second. The wing displacement is not magnified. All *continuous lines* are straight line segments between data points, with no curve fitting

Γ_{tot}, which is composed of two parts, the circulation of the leading edge vortex, Γ_{LEV}, which can be estimated, and the strength of the bound wing circulation Γ_{pot}, which cannot be measured directly (because it would require resolution of the velocity field and its gradients in the boundary layer all around the wing section contour), but is calculated by subtraction so that

$$\Gamma_{tot} = -\Gamma_{TEV} = \Gamma_{LEV} + \Gamma_{pot}. \tag{26}$$

The net effect, as explained in Muijres et al. (2008), is that the attached leading edge vortex increases the lift by 40%.

It was not possible to deduce this on-wing result based solely on the far-wake data of previous studies, but as Dickinson (2008) notes, the existence of a large-scale LEV on the bat wing is not that surprising given previous observations of thin wings of hawkmoths at the same Re (approximately 5,000) by Willmott et al (1997) and Bomphrey et al. (2005). The Strouhal number, $St = fA/U$, where f is the wingbeat frequency and A is the tip-to-tip wingbeat amplitude, lay between 0.3 and 1.3 in the hawkmoth experiments. For the bats at $U = 1$ m/s, it is

1.36. Note however, that the smoke trails of Willmott et al. and the PIV-derived results of Bomphrey et al. came from tethered animals; while there are few animal welfare requirements for invertebrates, it can also be difficult to encourage repeatable flight behaviour patterns.

4 Extensions and variations

In some respects the experiments described above are quite limited in technical ambition—they all derive from measurements of two velocity components in a plane (or rather a slab). This does not limit their application to two dimensional flows, because predictions, tests and measurements can be made in specific slices through arbitrarily complex three dimensional flows. The selection and prediction of quantities relies on the integrated theoretical models that guide the measurement strategy. Yet, as technological improvements accumulate, we may expect to see more examples of more sophisticated measurement of velocity and pressure fields and their associated forces. For example, Hedenström et al. (2008, in this volume) show time-resolved sequences of three-component stereo data that can be used to sample wake structures as they convect past a fixed measuring window in a mean flow. When such measurements can be combined with fine resolution close to solid boundaries (e.g. Fig. 11), then the previously-noted analyses of Noca et al. (1999) and van Oudheusden et al. (2007) can be extended to more complex, time-varying flows, past deformable boundaries. The application to animal flight investigations is obvious. We may also note the developments in combined computer simulations and simple experimental modelling of mechanical flapping wings, noting the recent work by Wang et al. (2004) and Kurtulus et al. (2008) as examples of a rapidly expanding literature.

The term vortex structure has been used rather loosely here as a shorthand for some clump of above-average amplitude vorticity. There are many more rigorous ways of defining an object that can be called a vortex (here we have simply referred to vorticity whenever possible). These include the various invariants of the velocity gradient tensor, such as the Q-criterion (Hunt et al. 1988) and a measure of the swirl strength (Zhou et al. 1999). Other variations have been proposed, for example by Jeong and Hussein (1995) and Chakraborty et al. (2005). Generally these methods then apply some kind of threshold criterion to state when a vortex is, or is not present. That criterion may be more or less subjective.

Although it is quite straightforward to apply these measures to PIV-generated data, the limited resolution (either in space, or in time, or both) means that the true complexity of small-scale structures is often greatly underestimated by PIV data. PIV investigations can very

usefully be combined with qualitative methods such as smoke or dye visualisation so that the particular subset of features visible in PIV can be placed in context. Bomphrey (2006) gives a comprehensive review of application of these methods in insect flight studies, and both the PIV and smoke trails illuminate different aspects.

The interpretation of smoke or dye trails is not completely straightforward, however, and in time-varying flows, they do not mark an instantaneous streamline, but represent a time history of particles that have passed the seeding point, or points. Classifications of smoke trails and instantaneous streamlines by critical points (Perry et al. 1980) and more rigorous identification in reduced forms of the velocity field (Chong et al. 1990) have been introduced, but most often smoke and dye visualisations are most useful for detailed, but qualitative information.

All of the above methods use an Eulerian description of the velocity field, and Haller (2005) has made the case that a more useful object in the flow might be the Lagrangian coherent structure (LCS), whose boundaries are determined by the rate of expansion of local fluid particles, as measured by a direct Lyapunov exponent (DLE). The DLE can be calculated quite readily from time-resolved PIV sequences, as noted in principle by Haller (2002), and the ridges or boundaries of high DLE separate significantly different parts of the flow (Shadden et al. 2005). Example descriptions of flow fields, including that of jellyfish locomotion, in these terms from time-resolved PIV data are given in Shadden et al. (2006) and Peng and Dabiri (2007). Green et al. (2007) apply the techniques to DNS of three dimensional fluid turbulence and Cardwell and Mohseni (2008) show an application to DNS data of the flow over a two dimensional Eppler 387 airfoil at fixed angle of attack at $Re = 6 \times 10^4$.

The continuing development of sophisticated analysis techniques that match the technology developments in lasers and digital cameras are signs of a very interesting near future.

5 Conclusions

The swift and bat studies reviewed above might best be regarded as combined experimental and theoretical studies, since the meaning or significance of the flowfield measurements can only be derived by combining with a theoretical model of some kind. Most PIV studies can in fact be regarded this way, as it is only when the numerous velocity vector fields can be placed in some predictive/theoretical context that they become something more than qualitative flow markers.

Particle image velocimetry measurement bandwidths are on the order of 100, which is low when compared with other velocity measurement techniques. The likely lower bound of the error in velocity measurement is usually a fixed multiple of the discrete sensor grid, and so cannot be expressed as a constant fraction of u_{obs}, but common estimates of $\pm 1\%$ in $\mathbf{u}$ and $\pm 5\%$ in gradient quantities should be regarded as target ideals in very well-controlled experiments. The art then lies in making a robust analysis that is not affected by predictable measurement error, and integral measures often achieve this.

Combinations of the integral and differential forms of the momentum equations can be used to calculate time-averaged or instantaneous forces. Estimating the pressure field is often the most difficult task, one that can be side-stepped by working far enough from the disturbance that the pressure gradients are small. Most of the examples have been for slices or slabs taken through the flow field, but extension to three dimensions is mainly constrained by the technology as the analysis principles are the same.

As time-resolved and three-dimensional data become more readily available, the volume of data will grow very fast, but special care will still have to be taken for the correct estimation of gradient quantities, particularly near moving and deformable boundaries.

References

Adrian RJ (2005) Twenty years of particle image velocimetry. Exp Fluids 39:159–169

Anderson JD (2001) Fundamentals of aerodynamics, 3rd edn. McGraw-Hill, New York

Betz AA (1925) A method for the direct determination of profile drag. Z Flug Motorluftschiffahrt 16:42

Bomphrey RJ (2006) Insects in flight: direct visualization and flow measurements. Bioinsp Biomim 1:S1–S9

Bomphrey RJ, Lawson NJ, Harding NJ, Taylor GK, Thomas ALR (2005) The aerodynamics of Manduca sexta: digital particle image velocimetry analysis of the leading-edge vortex. J Exp Biol 208:1079–1094

Bomphrey RJ, Taylor GK, Lawson NJ, Thomas ALR (2006) Digital particle image velocimetry measurements of the downwash distribution of a desert locust Schistocerca gregaria. J R Soc Interf 3:311–317

Cardwell BM, Mohseni C (2008) Vortex shedding over a two-dimensional airfoil: where the particles come from. AIAA J 46(3):545–547

Chakraborty P, Balachandar S, Adrian RJ (2005) On the relationships between local vortex identification schemes. J Fluid Mech 535:189–214

Chen J, Katz J (2005) Elimination of peak-locking error in PIV analysis using the correlation mapping method. Meas Sci Tech 16:1605–1618

Cholemari MR (2007) Modeling and correction of peak-locking in digital PIV. Exp Fluids 42:913–922

Chong MS, Perry AE, Cantwell BJ (1990) A general classification of three-dimensional flow fields. Phys Fluids A2(5):765–777

Dabiri JO (2005) On the estimation of swimming and flying forces from wake measurements. J Exp Biol 208:3519–3532

Dabiri JO, Colin SP, Costello JH (2006) Fast-swimming hydromedusae exploit velar kinematics to form an optimal vortex wake. J Exp Biol 209:2025–2033

Dickinson MH (2008) Animal locomotion: a new spin on bat flight. Curr Biol 18(11):R468–R470

Fincham AM, Spedding GR (1997) Low cost, high resolution DPIV for measurement of turbulent fluid flow. Exp Fluids 23:449–462

Fincham AM, Delerce G (2000) Advanced optimization of correlation imaging velocimetry algorithms. Exp Fluids 29:S13–S22

Green MA, Rowley CW, Haller G (2007) Detection of Lagrangian coherent structures in three-dimensional turbulence. J Fluid Mech 572:111–120

Haller G (2002) Lagrangian coherent structures from approximate velocity data. Phys Fluids 14(6):1851–1861

Haller G (2005) An objective definition of a vortex. J Fluid Mech 525:1–26

Hedenström A, van Griethuijsen L, Rosén M, Spedding GR (2006) Vortex wakes of birds: recent developments using digital particle image velocimetry in a wind tunnel. Anim Biol 56:535–549

Hedenström A, Johansson LC, Wolf M, von Busse R, Winter Y, Spedding GR (2007) Bat flight generates complex aerodynamic tracks. Science 316:894–897

Hedenström A, Muijres F, von Busse R, Johansson C, Winter Y, Spedding GR (2008) High-speed 3D PIV measurements of bat wakes flying freely in a wind tunnel. Exp Fluids (submitted, this volume)

Hedenström A, Spedding GR (2008) Beyond robins: aerodynamic analyses of animal flight. J R Soc Interf 5:595–601

Henningsson P, Spedding GR, Hedenström A (2008) Vortex wake and flight kinematics of a swift in cruising flight in a wind tunnel. J Exp Biol 211:717–730

Huang HT, Fiedler HE, Wang JJ (1993) Limitation and improvement of PIV. Part II: particle image distortion, a novel technique. Exp Fluids 15:263–273

Hunt JCR, Wray AA, Moin P (1988) Eddies, stream, and convergence zones in turbulent flows. Center for Turbulence Research Report CTR-S88, Stanford

Jeong J, Hussein F (1995) On the identification of a vortex. J Fluid Mech 285:69–94

Kester W (2006) ADC input noise: the good, the bad and the ugly. Is no noise good noise? Analog Dialogue 40(02):13–17

Kurtulus DF, David L, Farcy A, Alemdaroglu N (2008) Aerodynamic characteristics of flapping motion in hover. Exp Fluids 44:23–36

Lighthill MJ (1970) Aquatic animal propulsion of high hydromechanical efficiency. J Fluid Mech 44:265–301

Lin JC, Rockwell D (1996) Force identification by vorticity fields: techniques based on flow imaging. J Fluids Struct 10:663–668

Meheut M, Bailly D (2008) Drag-breakdown methods from wake measurements. AIAA J 46(4):847–863

Muijres FT, Johansson LC, Barfield R, Wolf M, Spedding GR, Hedenström A (2008) Leading-edge vortices increase lift in bat flight. Science 319:1250–1253

Noca F, Shiels D, Jeon D (1999) A comparison of methods for evaluating time-dependent fluid dynamic forces on bodies, using only velocity fields and their derivatives. J Fluids Struct 13:551–578

Nogueria J, Lecuona A, Rodriguez PA (2001) Identification of a new source of peak locking, analysis and its removal in conventional and super-resolution PIV techniques. Exp Fluids 30:309–316

Norberg UM (1990) Vertebrate flight. Springer, Berlin

Peng J, Dabiri JO (2007) A potential flow, deformable-body model for fluid structure interactions with compact vorticity: application to animal swimming measurements. Exp Fluids 43:655–664

Perry AE, Lim TT, Chong MS (1980) The instantaneous velocity fields of coherent structures in coflowing jets and wakes. J Fluid Mech 101:243–256

Polhamus EC (1971) Predictions of vortex-lift characteristics by a leading-edge suction analogy. J Aircraft 8(4):193–199

Prandtl L, Tietjens OG (1934) Applied hydro- and aeromechanics. United Engineering Trustees and Dover Publications, New York

Prasad AK, Adrian RJ, Landreth CC, Offutt PW (1992) Effect of resolution on the speed and accuracy of particle image velocimetry interrogation. Exp Fluids 13:105–116

Saffman PG (1970) The velocity of viscous vortex rings. SIAM J 49:371–380

Saffman PG (1992) Vortex dynamics. Cambridge University Press, Cambridge, UK

Scarano F (2002) Iterative image deformation methods in PIV. Meas Sci Tech 13:R1–R19

Scarano F, Riethmuller ML (1999) Iterative multigrid approach in PIV image processing with discrete window offset. Exp Fluids 26:513–523

Shadden S, Lekien F, Marsden J (2005) Definition and properties of Lagrangian coherent structures from finite-time Lyapunov exponents in two-dimensional aperiodic flows. Physica D 212:271–304

Shadden S, Dabiri J, Marsden J (2006) Lagrangian analysis of fluid transport in empirical vortex ring flows. Phys Fluids 18:047105

Stanislas M, Okamoto K, Kahler CJ, Westerweel J, Scarano F (2008) Main results of the third international PIV challenge. Exp Fluids 45:27–71

Utami T, Blackwelder RF (1991) A cross-correlation technique for velocity field extraction from particulate visualization. Exp Fluids 10:213–223

van Oudheusden BW, Scarano F, Roosenboom EWM, Casimiri EWF, Souverein LJ (2007) Evaluation of integral forces and pressure fields from planar velocimetry data for incompressible and compressible flows. Exp Fluids 43:153–162

Wang ZJ, Birch JM, Dickinson MH (2004) Unsteady forces and flows in low Reynolds number hovering flight: two-dimensional computations vs robotic wing experiments. J Exp Biol 207:449–460

Westerweel J (1997) Fundamentals of digital particle image velocimetry. Meas Sci Tech 8:1379–1392

Westerweel J (2000) Theoretical analysis of the measurement precision in particle image velocimetry. Exp Fluids 29:S3–S12

White FM (2008) Fluid mechanics, 6th edn. McGraw-Hill, New York

Willert CE, Gharib M (1991) Digital particle image velocimetry. Exp Fluids 10:181–193

Willmott AP, Ellington CP, Thomas ALR (1997) Flow visualization and unsteady aerodynamics in the flight of the hawkmoth Manduca sexta. Phil Trans R Soc Lond B 352:303–316

Zhou J, Adrian RJ, Balachandar S, Kendall TM (1999) Mechanisms for generating coherent packets of hairpin vortices in channel flow. J Fluid Mech 387:353–396